Surfaces and Interfaces 34 (2022) 102377

Contents lists available at ScienceDirect

Surfaces and Interfaces

journal homepage: www.sciencedirect.com/journal/surfaces-and-interfaces

Comprehensive investigation of Er_2O_3 thin films grown with different ALD approaches

L. Khomenkova [a,d,e,*], H. Merabet [b], M.-P. Chauvat [a], C. Frilay [a], X. Portier [a], C. Labbe [a], P. Marie [a], J. Cardin [a], S. Boudin [c], J.-M. Rueff [c], F. Gourbilleau [a,*]

[a] CIMAP, CNRS, ENSICAEN, UNICAEN, CEA, Normandie Université, 6 Boulevard Maréchal Juin, Caen 14050 CEDEX 4, France
[b] Physics Program, Department of Mathematics, Statistics, and Physics, College of Arts and Sciences, Qatar University, P.O. box 2713, Doha, Qatar
[c] Normandie Univ., ENSICAEN, UNICAEN, CNRS, CRISMAT, 14000 Caen, France
[d] V. Lashkaryov Institute of Semiconductor Physics at the National Academy of Sciences of Ukraine, 45 Pr.Nauky, Kyiv 03028, Ukraine
[e] National University of Kyiv-Mohyla Academy, 2 Skovorody str., Kyiv 04070, Ukraine

ARTICLE INFO

Keywords:
Er_2O_3 thin films
Atomic layer deposition
TEM
XRD
Luminescence
Er silicate

ABSTRACT

The effect of Er precursor nature ($Er(CpMe)_3$ or $Er(tmhd)_3$) and annealing treatment at 500–1100 °C on the structural and optical properties of Er_2O_3 films grown on Si substrates by thermal or O_2-plasma-assisted atomic layer deposition was studied by means of spectroscopic ellipsometry, Fourier-transform infrared spectroscopy, X-ray diffraction, transmission electron microscopy coupled with energy dispersive X-ray spectroscopy as well as photoluminescence method. An annealing at 500–800 °C resulted in the film crystallization mainly. Thermal treatment at high temperatures caused the formation of Er silicate phase due to the diffusion of Si atoms from the substrate in the films depth. This phase was found to be Er_2SiO_5 being crystallized at 1100 °C. Light emitting properties of the films are determined by Er_2O_3 native defects (like oxygen vacancies) and intra-4*f* shell transition in Er^{3+} ions. The latter dominated in the films annealed at 1000–1100 °C. The most intense Er^{3+} emission, observed in the films grown with O_2-plasma-assisted approach, was explained by a lower contribution of oxygen vacancies as well as by pronounced crystallization of Er silicate phase. In this latter, the effect of concentration quenching of Er^{3+} luminescence was lower due to a larger distance between Er^{3+} neighbor ions.

1. Introduction

Over the last decades, atomic layer deposition (*ALD*) is widely used due to continuous downscaling of electronic devices as well as to the development of 3D-integrating circuits [1,2]. This technique allows forming thin films of different materials not only on flat substrates, but also on complex 3D-surfaces and structures at relatively low temperatures [3,4]. The films with specific chemical composition can be easily deposited via alternating exposure of gaseous chemical precursors and reactants. Due to self-limiting saturated reactions, the thickness of the films and their composition can be controlled via repetition of different *ALD* cycles. The slow growth of *ALD* films, that is usually caused by an incomplete removing of large molecular groups or generated by-products, is no longer an hindrance as traditional coating processes because of fine tuning of film thickness at a sub-nanometer scale.

Nowadays, rare earth sesquioxides and materials on their basis attract considerable attention because of their wide range of applications such as optical devices, microelectronics, magnetic devices, photonics and photovoltaics. These oxides are known to exist in three main polymorphs, i.e. hexagonal, monoclinic and cubic bixbyite structures (so-called, A-, B- and C-forms, respectively) [5]. Different research groups reported on the growth of these materials on different semiconducting substrates including C-Sc_2O_3/GaN [6,7], La_2O_3/Si [8], Pr_2O_3/Si [9], Sm_2O_3/Si [10], C-Er_2O_3/Si [11,12], C-Er_2O_3/GaN [13], Yb_2O_3/Si [14], etc.

It is known that Er_2O_3 has good heat endurance and chemical durability under high temperatures that makes it attractive for the protection and anticorrosion coating of steels [15]. Due to its high dielectric constant, Er_2O_3 is applicable also for gate insulators [16,17]. Owing to intense photoluminescence at room temperature, Er_2O_3 materials can be used for the fabrication of high-gain optical waveguide amplifiers and optoelectronic integrated circuits [18,19].

Abbreviations: TEM, Transmission electron microscopy; XRD, X-ray diffraction; ALD, Atomic layer deposition.

* Corresponding authors at: CIMAP, ENSICAEN, UNICAEN, CEA, CNRS, Normandie Université, 6 Boulevard Maréchal Juin, Caen 14050 CEDEX 4, France.
E-mail addresses: khomen@ukr.net (L. Khomenkova), fabrice.gourbilleau@ensicaen.fr (F. Gourbilleau).

https://doi.org/10.1016/j.surfin.2022.102377
Received 6 November 2021; Received in revised form 15 May 2022; Accepted 23 September 2022
Available online 28 September 2022

The methods of Er_2O_3 thin film deposition include physical vapor deposition [18,20,21], chemical vapor deposition [11,22], sol-gel method [23], magnetron sputtering [11,24,25] and, more recently, *ALD* technique [12,26].

In this work, Er_2O_3 films were grown on Si substrates by either thermal or plasma-assisted *ALD* approaches. Hereafter, the effect of deposition conditions and post-deposition treatments on the optical, structural and luminescent properties of these films will be compared and discussed.

2. Experimental details

The Er_2O_3 thin films were grown using two Er precursors, i.e. Er $(CpMe)_3$ (tris(methylcyclopentadienyl)erbium(III) (99.9%-Er), CAS No. 39470-10-5, chemical formula $Er(CH_3C_5H_4)_3$, formula weight 404.62 g/mol) and $Er(tmhd)_3$ (tris(2,2,6,6-tetramethyl-3,5-heptanedionato) erbium(III), 99% (99.9%-Er), CAS No. 35733-23-4, chemical formula Er $(C_{11}H_{19}O_2)_3$, formula weight 717.08 g/mol). Both precursors were provided by STREM Chemicals Inc. [27].

2.1. Properties of Er precursors

Prior to install Er precursors in the *ALD* deposition tool, they were submitted to thermogravimetric analysis (*TGA*) using a SETERAM TAG 92 setup. The measurements were done under air atmosphere at a heating rate of 3°C/min from room temperature to 800°C. The *TG* curves obtained for both Er precursors, $Er(CpMe)_3$ and $Er(tmhd)_3$, at atmospheric pressure show different profiles (Fig. 1,a). The $Er(CpMe)_3$ precursor exhibits a continuous weight loss in the 25–800 °C temperature range with a final weight loss of 51.7 % which is in good agreement with the theoretical value of 52.7% expected for the formation of Er_2O_3.

Regarding the $Er(tmhd)_3$ precursor, this material shows a three-step degradation process with temperature. Between 25 and 170 °C the *TG* curve presents a plateau showing that the precursor is stable in this temperature range. Above 170 °C and up to 318 °C, a first weight loss of 87% is observed immediately followed by a second mass loss of 7.25% up to 800 °C. Contrary to the $Er(CpMe)_3$ compound, the final weight loss of 94.25 % for $Er(tmhd)_3$ at 800 °C is much more important than the theoretical value of 73.3% expected for the formation of Er_2O_3. This mass difference (Δm = 20.95%) can be explained by the concomitant decomposition and sublimation-vaporization of $Er(tmhd)_3$ which both contribute to the weight loss during *TGA* study due to the volatility of (tmhd)-chelates of rare earths [28].

The *XRD* analysis performed for both precursors before and after *TG* experiments showed that initial $Er(tmhd)_3$ precursor presents a crystalline structure whereas $Er(CpMe)_3$ is amorphous (Fig. 1,b). The final material obtained after *TGA* for both precursors (Fig. 1,b) was identified as Er_2O_3 oxide in its cubic phase [29,30].

It should be emphasized that thermal behavior of both Er precursors was extracted from the *TG* experiment performed in air atmosphere at ambient pressure. This fact can explain some difference in mass loss in comparison with the results reported for the similar precursors by other groups [[12,31]. The multi-step mass loss upon the heating is the evidence of precursors' decomposition via step-like desorption of corresponding organic ligands. Similar effect was previously described, for instance, for Cp-based Zr precursors [32,33] and explained by the difference in interactions in the gas phase in *TG* experiment and on the surface of condensed phase during the *ALD* process.

Successful deposition of the films using *ALD* technique depends on many parameters such as substrate temperature, pulse/purge duration of the precursor and the oxidant, flow of vector-gas, chamber pressure, etc. Their effect on the film growth is considered below.

2.2. Samples

Er_2O_3 thin films were grown using a Picosun® R-200 Advanced deposition tool from Picosun Oy company (Finland) [34]. P-type (B-doped) Si wafers grown by Czochralski pulling technique produced by "Sil'tronix Silicon Technologies" company (France) were used [35]. The wafers, being of (100) orientation and double side polished, had the following dimensions: 2 inches in diameter and 275 ± 25 μm in thickness. Their resistivity was ρ = 15 Ω·cm. The virgin substrates were covered with a 5-nm thermal SiO_2 layer.

$Er(CpMe)_3$ and $Er(tmhd)_3$ precursors were introduced in the *ALD*

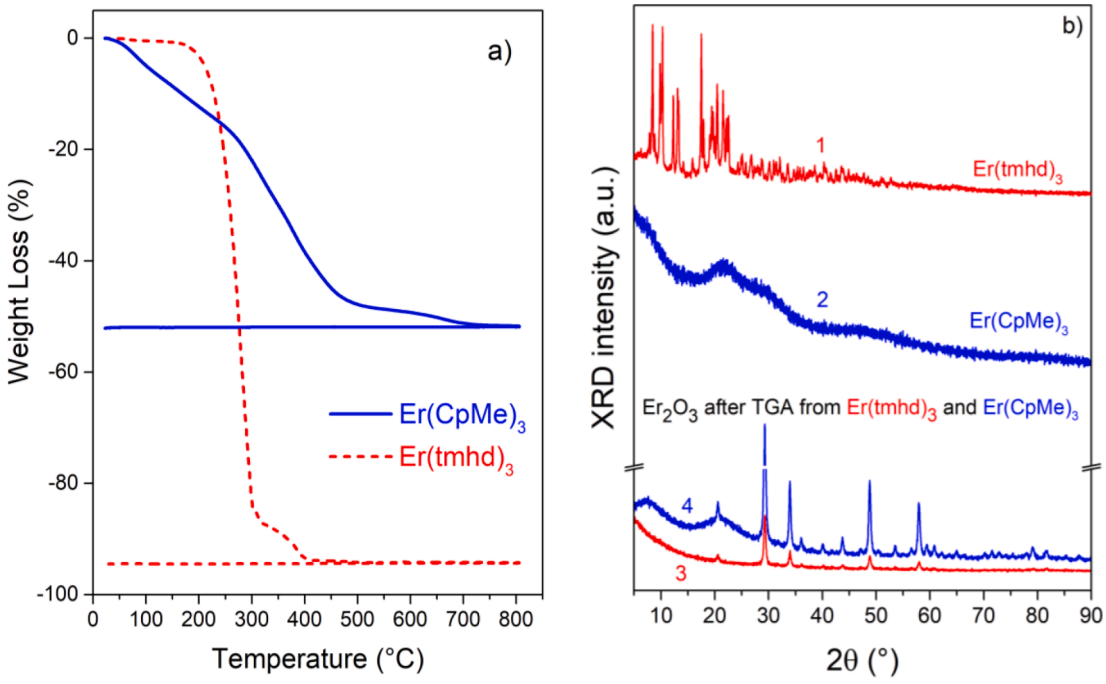

Fig. 1. (a) Weight loss as a function of temperature for $Er(tmhd)_3$ and $Er(CpMe)_3$ precursors; (b) XRD patterns recorded on $Er(tmhd)_3$ (1,3) and $Er(CpMe)_3$ (2,4) precursors before (1,2) and after (3,4) thermogravimetric experiments.

reactor from outside containers with the flow of 150 sccm. Nitrogen (99.999 %) was used as a carrier and purge gas. The main deposition parameters are collected in Table 1S (see electronic supplement information).

Thermal *ALD* deposition was performed with $Er(CpMe)_3$ precursor and distilled water used as oxidant. The water container was kept at 25 °C. The temperature of the bottle with $Er(CpMe)_3$ was varied in the range T_b = 120–200 °C. The value of T_b = 200 °C was the highest reachable for bottle configuration in our deposition tool. The pulse/purge durations for $Er(CpMe)_3$ were varied in the range of t_{pulse} = 1-3 s and t_{purge} = 2–6 s. The precursor flow was 150 sccm. To increase the amount of the precursor in the reaction zone, the boost was used with the flow varied from 250 to 800 sccm. The water flow was kept as 150 sccm and pulse/purge durations were fixed at t_{pulse} = 0.1 s and t_{purge} = 4 s.

Plasma-assisted *ALD* process was carried out with $Er(tmhd)_3$ and oxygen plasma. A container with $Er(tmhd)_3$ was heated at T_b = 155–200 °C. Corresponding $Er(tmhd)_3$ pulse/purge time were t_{pulse} = 2–4 s and t_{purge} = 4–6 s. Oxygen plasma was introduced in the reactor with a flow of 150 sccm and the pulse/purge times of t_{pulse}=13–56 and t_{purge} = 2–4 s. The radio-frequency plasma power (*RFP*) and its duration were varied in the 1500–3000 W and 10–52 s ranges, respectively.

The substrate temperature was tuned in the T_d = 275–325 °C range for both approaches. The film thickness was controlled via the cycles' number.

After the evacuation of the substrates with uniformly deposited films from the *ALD* tool, they were cut into small pieces (called hereafter as samples) and submitted to annealing treatment at different temperatures (T_A = 500–1100 °C) and durations (t_A = 10–30 min) in nitrogen atmosphere.

2.3. Experimental techniques used for the film characterization

To investigate optical, structural and luminescent properties of the films versus annealing treatment, several techniques were used. The spectroscopic ellipsometry study was performed using a Jobin-Yvon ellipsometer (UVISEL, HORIBA Ltd., Kyoto, Japan). The incident light was scanned in the 1.5–6.0 eV range and incident angles were 65°, 70° and 75°. The beam spot was 1 mm in diameter. The spectra were recorded from the central point of each sample.

The surface of the films was analysed by means of optical microscopy using Olympus microscope and atomic-force microscopy (*AFM*) using the NanoScope® III Scanning probe microscope (Digital Instruments) operated in amplitude and phase tapping modes.

Vibrational properties of the films were investigated using Fourier transform infrared spectroscopy (*FTIR*). The *FTIR* absorption spectra were recorded with a Nicolet™ iS50 *FTIR* spectrometer with normal and 60° incidence of excitation light.

Structural properties of the films were studied using X-ray reflectivity and X-ray diffraction methods. The *XRD* data were collected using X-ray diffractometer Philips X'Pert-MRD with the Cu $K\alpha_1$ radiation (λ = 0.15418 nm) or Co $K\alpha_1$ radiation (λ = 0.17889 nm). The patterns were recorded in Bragg-Brentano (θ-2θ) and grazing (ω-2θ) geometries.

For Transmission Electron Microscopy (*TEM*) observations, the cross sectional thin foils of the films were prepared by *FIB* (Focused Ion Beam) such that the *TEM* observations were done following a [110] direction of the (100) Si substrate. In such a way, the electron beam was parallel to the film/substrate interface. The *FIB* system used was a Dual beam FEI Helios nanolab660 with an electron imaging resolution of 0.6 nm at 15 kV (Field Emission Gun - *FEG*) and a *FIB* resolution of 2.54 nm at 30 kV. In order to protect the film surface from the gallium ion beam during the thinning process, a carbon deposit was carried out beforehand as well as two platinum layers deposited electronically (0.3 μm) and then ionically (2 μm). The thinning was processed by a set of repetitive inclinations of the gallium beam (±1° with decreasing gradually the beam currents in the first phases and a final surface cleaning step with a higher inclination but for lower currents) on either side of the thin section until electron transparency (a few tens of nanometers). The conventional bright and dark fields (*CTEM*) and high resolution *TEM* (*HRTEM*) observations, scanning transmission electron microscopy and high angle annular dark field *(STEM-HAADF*) observations as well as *STEM-EDX* chemical imaging were performed using a JEOL ARM200F microscope with a "cold" field emission gun (*FEG* - 200 kV) and having the double corrections of aberrations in image and in *STEM* modes. The point to point resolutions were 0.1 nm in *TEM* mode and 0.078 nm in *STEM-HAADF* mode. This microscope was equipped with an *EDX* Centurio JEOL spectrometer. All digital images were processed with the GMS2 GATAN Digital Micrograph software.

Raman scattering spectra were recorded in a quasi-backscattering geometry using a Jobin Yvon LabRaman 300 spectrometer with a resolution of 1.57 cm^{-1}, equipped with a confocal microprobe and a *CCD* camera. As an excitation source, the second harmonic of Nd:YAG laser (532 nm) was used. The laser beam power was around 1.5 mW and the spot diameter was 0.87 μm. Under such conditions, no heating of the sample was observed during spectra recording. This setup was also used to collect micro-photoluminescence spectra. Besides, standard *PL* and *PL Excitation* (*PLE*) spectra were measured with Horiba Fluorolog-3 setup (model FL3-22). It is equipped with a 450-W Xenon light source, double-grating excitation and emission spectrometers of Czerny-Turner design with kinematic classically-ruled gratings and all-reflective optics, with automated slits, and room-temperature R928P detector. A 2-nm band-pass is achieved using 1200-grooves/mm gratings with a dispersion of 2.1 nm/mm and a 1 mm slits. Calibrated photodiode is used for excitation correction from 240-1000 nm. Emission detector is an R928P for high sensitivity in photon-counting mode in the 240–850 nm spectral range. To record Er^{3+} photoluminescence in infrared spectral range, a Jobin Yvon 1 m single grating monochromator equipped with Hamamtsu detector was used. The excitation was performed using a 488-nm line of Ar^+ laser. The *PL* and *PLE* spectra were corrected automatically with dedicated software during spectra recording. The measurements were performed at room temperature.

3. Experimental results and discussion

3.1. Parameters of the films obtained from spectroscopic ellipsometry

Spectroscopic ellipsometry is known as a fast, sensitive and non-destructive method for the investigation of optical properties of thin films. Hereafter we used an approach described in details in our previous works [36–38]. In brief, a spectrum consists in the measured Ψ and Δ ellipsometric angles defined from the fundamental equation $\bar{r}_p/\bar{r}_s = \tan\Psi\cdot\exp(i\Delta)$, where $\bar{r}_p$ and $\bar{r}_s$ are the complex reflection coefficients for parallel and perpendicular polarizations of light, respectively. The light intensity in both polarizations is considered as $I_s = I\cdot\sin2\Psi\cdot\sin\Delta$ and $I_c = I\cdot\sin2\Psi\cdot\cos\Delta$. For ellipsometric modeling of a rough film, this latter is divided it into two parts: one part containing the homogeneous film and the other part representing a non-homogeneous form referred to as "roughness layer". The first part is simulated with the physically meaningful dielectric function belonging to the material. To model the film roughness, Maxwell-Garnett effective medium approximation was applied. This approach allowed to obtain self-agreed results not only for as-deposited, but also for the films annealed, especially, at high temperatures. The roughness value of the films (R_f) estimated from one ellipsometric spectrum is considered as a mean height calculated over the entire measured surface illuminated by excitation light in one run that corresponding to the beam spot size.

Fig. 2,a shows typical spectra and their modeling applying a "new-amorphous" model described recently in Refs.[36–38]. The use of three different angles of incident light improves the accuracy for the determination of the film thickness, *d*, and film roughness, as well as refractive index, *n*, and the absorption coefficient, α (if any). By the

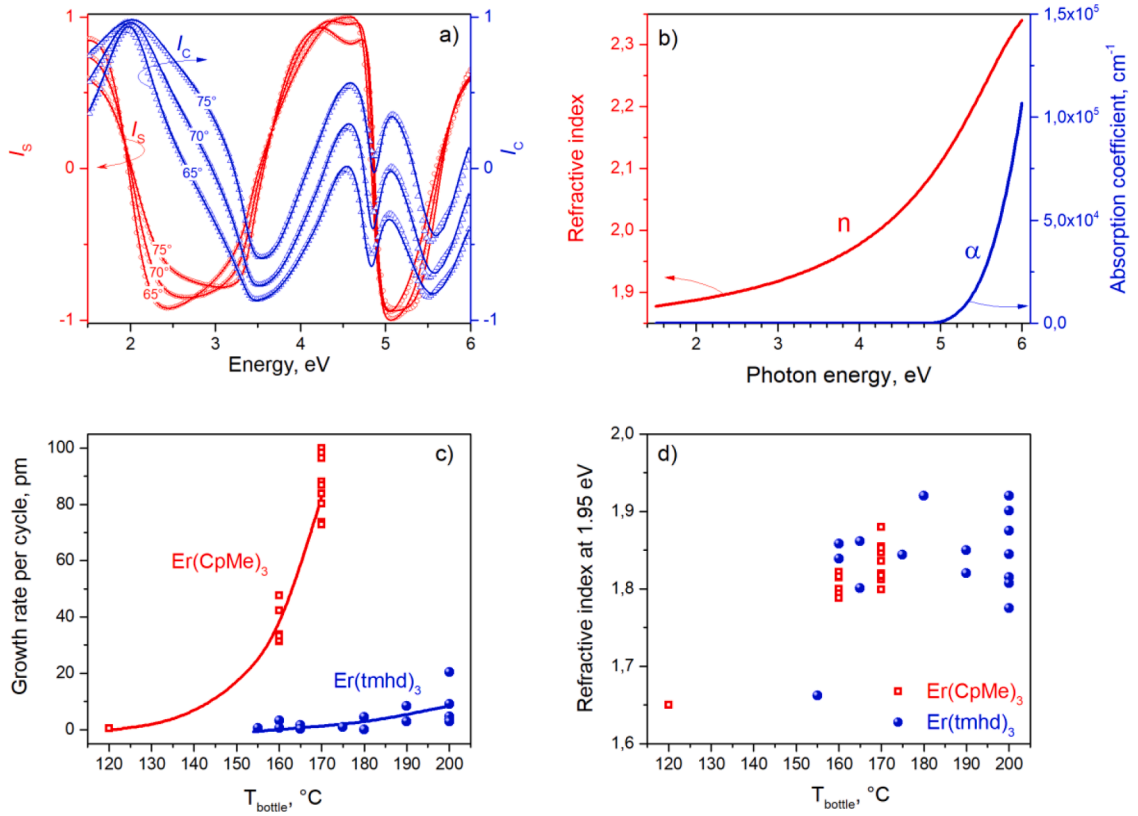

Fig. 2. (a) Typical ellipsometry spectra for as-deposited Er_2O_3 film (symbols) taken at 65°, 70° and 75° and their fitting (solid curves) using "new amorphous" model. (b) Refractive index and absorption coefficient of as-deposited Er_2O_3 film extracted from the fitting of experimental data in a). (c, d) the effect of bottle temperature on film growth rate per cycle (c) and refractive index (d) for the films deposited with thermal and plasma-assisted approaches using $Er(CpMe)_3$ and $Er(tmhd)_3$ precursors, respectively. RFP = 2000 W (c, d) for $Er(tmhd)_3$. The different points for the same deposition temperature originate from the different precursor pulse/purge times.

fitting of ellipsometry spectra, typical dispersion law was obtained along with the variation of absorption coefficient (Fig. 2,b). The analysis of spectral dependence of absorption coefficient permits to estimate the bandgap energy (E_g) of Er_2O_3 films. For this purpose, the Tauc relation between the absorption coefficient (α) and the bandgap (E_g) $\alpha h\nu = A*(h\nu - E_g)^m$, where $h\nu$ is the photon energy, A is a constant, and m is a constant that depends on the type of transitions involved, i.e. $m = 1/2$, 3/2, 2 and 3 corresponds to direct allowed, direct forbidden, indirect allowed and indirect forbidden transitions, respectively. It was reported that the the energy of direct bandgap may represent the onset of intrinsic absorption of the oxide, while the the energy of indirect bandgap may represent the onset of absorption involving some defect states [39]. Thus, the plotting of these dependencies permits to get information on the bandgap value and defects in our materials. The direct energy gap was obtained by plotting $(\alpha h\nu)^2$ versus $h\nu$ (Fig. 5S,a) whereas the indirect energy gap was obtained by plotting $(\alpha h\nu)^{1/2}$ versus $h\nu$ (Fig.5S,b). It turned out that in the first case $E_g \sim 5.76$ eV and in the latter case – $E_g \sim$ 5.2 eV that is in agreement with the data reported in [10,39–41].

The growth rate per cycle, r_G, and corresponding n values were analyzed versus different deposition conditions. For all the films, the effects of the substrate temperature, temperature of bottle with Er precursor, and pulse/purge time for Er precursor and oxidant were considered. Along with this, for thermal *ALD*, the effect of the boost flow of Er precursor was studied, whereas for the plasma-enhanced *ALD*, the influence of oxygen plasma power (*RFP*) and duration of its application was investigated. The obtained results are collected in Figs. 1S–4S.

It turned out that for the *films grown with plasma-assisted ALD,* the start of film growth with the $r_G = 0.5$ pm/cycle occurs when $T_b = 155$ °C (Fig. 2,c). Further T_b rise up to 200 °C results in the r_G rise. Depending on the $Er(tmhd)_3$ and O_2 pulse/purge durations, the r_G can reach the values from 9 to 20 pm/cycle, being higher for shorter Er pulse time (Fig. 1S). The decrease of O_2 pulse time brings the same result due to incomplete oxidation of Er precursor. It is worth to point out that the $T_b = 200$ °C value for the $Er(tmhd)_3$ cylinder exceeds significantly the values reported for similar Er compounds in [12] that could be caused by the difference in the configuration of the cylinders used in [12] and in our *ALD* unit.

The r_G value has a non-monotonic behavior versus oxygen plasma power (Fig. 2S). The highest value of about 20 pm/cycle is obtained for *RFP* =2000 W. This *RFP* value was kept for further production of the films with plasma-assisted approach.

The refractive index of the films deposited at $T_b = 200$ °C is found to be in the range of n =1.75–1.92 showing a trend to decrease with Er pulse time rise (Figs. 2,d, 1S). The obtained values are in good agreement with those reported in the literature for Er_2O_3 [5,40].

For the films grown with thermal ALD approach, no deposition is observed for $T_b < 120$ °C. For $T_b = 120$ °C, the appearance of the film with r_G 0.5 pm/cycle is detected (Fig. 2,c). Further T_b increase up to 170 °C results in the r_G increasing up to 80–100 pm/cycle whereas at higher T_b, the r_G decreases dramatically and for $T_b = 190$–200 °C no film is obtained (Figs. 2,c, 3S).

The highest r_G values of about 80-100 pm/cycle was achieved for the films deposited with $T_b = 170$ °C and t_{pulse}/t_{purge} = (1.6–2.0)s/4s (Figs. 2, c, 3S). The refractive index for these films measured at 1.95 eV is found to be n = 1.8–1.87 being similar to the value observed for films grown with the plasma-assisted approach. It should be noted that further T_b increase up to 175–180 °C caused the crystallization of $Er(CpMe)_3$ precursor inside the cylinder and, as a consequence, no film deposition on substrate. The increase of the $Er(CpMe)_3$ pulse time from 1.6 s up to 2 s results in the slight increase of growth rate, whereas further pulse time

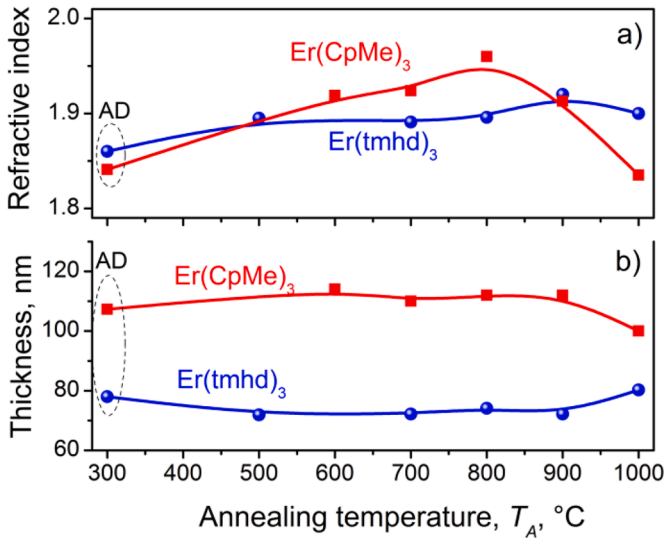

Fig. 3. (a) Evolution of the refractive index (at 1.95 eV) and (b) thickness of the films grown with the thermal approach (square symbols) and the plasma-assisted approach (circle symbols) with annealing temperature T_A. The symbols marked by "AD" and dashed lines at $T = 300$ °C correspond to the thickness and refractive index of as-deposited films that have been grown at 300 °C.

rise up to 4 s did not change it (Fig. 3S)

Analysis of the effect of deposition conditions reveals a low refractive index ($n = 1.65$) for the films grown from $Er(CpMe)_3$ with $T_b = 120$ °C and from $Er(tmhd)_3$ with $T_b = 155$ °C. The lowering of the n value can be caused by the presence of a phase with lower refractive index in the film due to incomplete Er precursor oxidation and/or presence of byproducts, as well as the formation of SiO_x or $ErSiO_x$ layer on the substrate surface instead of Er_2O_3 film in contrast to the results reported in [12] where stoichiometric Er_2O_3 films were obtained.

The effect of substrate temperature on the growth rate and optical properties of the films was also studied. The optimal deposition temperature is determined as T_d=300°C which allowed achieving high growth rate for both approaches. Taking into account the results described above, the effect of annealing treatment on the properties of the films grown with thermal *ALD* approach (with $T_d = 300$ °C, $T_b = 170$ °C, $Er(CpMe)_3/H_2O$ pulse/purge time as 1.6s/2.0s/0.1s/2.0s) and by plasma-assisted deposition (with $T_d = 300$ °C, $T_b = 200$ °C, $Er(tmhd)_3/O_2$ plasma pulse/purge time as 2.0s/4.0s/26.0s/4.0s) will be discussed in details.

3.2. *Effect of annealing treatment on film thickness and refractive index*

Fig. 3 represents the effect of annealing temperature on the refractive index at 1.95 eV (Fig. 3,a) and thickness (Fig. 3,b) of the films produced with the two different approaches. It is seen that, the refractive index of as-deposited films *grown with the plasma-assisted approach* is about $n = 1.860$ (at 300 °C). As evidenced, the annealing treatment does not modify greatly the values of the refractive index as well as the thickness of the film. By contrast, annealing at $T_A = 500$ °C results in the slight increase of the n up to 1.896 that remains almost constant with T_A rise up to 800 °C. For $T_A = 900$ °C, the refractive index reaches n =1.920, while further T_A rise up to 1000 °C causes some decrease of n down to 1.90. At the same time, the thickness of the film decreases slightly when $T_A = 500$ °C and does not change up to $T_A = 900$ °C. Such a behavior can be ascribed to the densification of the film and its crystallization. For $T_A = 1000$ °C, the film thickness becomes larger, but does not exceed the thickness of the as-deposited film. Taking into account some decrease of the refractive index along with the film thickening for $T_A = 1000$ °C, one can suppose that the formation of a phase with lower refractive index (for instance, SiO_x or $ErSiO_x$ as well as cavities) can occur upon annealing.

The *films, prepared with the thermal approach*, demonstrate pronounced variation of the refractive index and thickness with annealing treatment. With T_A rise up to 800 °C, the n value evolves from 1.84 (as-deposited at 300°C) up to 1.95 ($T_A = 800$ °C). Simultaneously, the thickness of the film increases from 108 up to 115 nm ($T_A = 500$ °C) and does not change up to $T_A = 800$–900 °C. The increase of the refractive index with a concomitant unchangeable thickness of the film can be ascribed to the film crystallization. However, further T_A increase up to 1000 °C results in the decrease of refractive index down to $n = 1.83$ accompanied by the decrease of film thickness. This behavior can be caused by the formation of cavities along with an increasing SiO_2 interfacial layer thickness as well as a possible appearance of Er silicate phases.

To obtain more information about structural variation and possible formation of pores and/or Si-rich phases, the samples were studied with *FTIR* and *XRD* methods as well as different electron microscopy techniques.

3.3. *Effect of annealing on structural properties of the films*

3.3.1. *AFM data*

All the films described above were observed using optical and atomic force microscopy methods. Fig. 4,a–c show the surface morphology of Er_2O_3 films grown with *the thermal approach and annealed at different temperatures*. It is seen that as-deposited film has a smooth surface that is free of any structural elements (Fig. 4,a).

Annealing results in the appearance of some contrasts on the film surface as well as formation of holes and/or cracks (Fig. 4,b and c). These latter are observed in small quantities for the films heated at $T_A = 600$ °C (Fig. 4,b), while annealing at $T_A = 900$ °C results in the formation of a crack network (Fig. 4,c). Further T_A increase (up to 1000 °C) causes the development of the holes and cracks as well as the increase of their depth. This structure evolution was found to be similar to the data reported in Ref. [41].

The surface of the samples prepared with *plasma assisted approach* is found to be smooth both for as-deposited samples and those annealed at $T_A \leq 800$ °C (Fig. 4,d and f). No cracks were found in such films whatever the T_A value. For $T_A = 900$–1000 °C, a modification of the surface morphology occurs (Fig. 4, f). However, these transformations are less significant than for the films grown with the thermal approach. These findings are confirmed by observations of the same samples with *AFM* method and presented hereafter.

Fig. 5 represents *AFM* images of the surface of the films annealed at high temperatures ($T_A = 900$ and 1000 °C). It is seen that the surface of the films, grown with the plasma-assisted approach and annealed at 900°C, presents structural elements (or grains).

The analysis of *AFM* image over 2 × 2 μm^2 surface (Fig. 5,a) shows that these grains have lateral and vertical sizes in the range 20–140 nm and 3–10 nm, respectively. The root-mean square roughness (*RMS*) is about 1.03 nm. Annealing at $T_A = 1000$ °C results in the *RMS* increase up to 1.39 nm. The lateral sizes of the elements (grains) rise up to 50–170 nm, whereas their height is still in the 5–10 nm range (Fig. 5,b).

AFM study of the films grown with thermal *ALD* approach revealed also that heat treatment caused not only the appearance of the grains on film surface, but also the development of a crack network (Fig. 5,c). Indeed, for the films annealed at $T_A = 900$ °C, for the observed regions, grains with lateral sizes of 20–200 nm and height of 3–8 nm are detected, whereas the width of the cracks is 25–100 nm. As for the crack depth, its value is found to be between 10 and 25 nm. However, one can note that the cracks could be deeper, but AFM tip cannot penetrate in the crack depth due to its physical size. The *RMS* value was 2.61 nm (over 2 × 2 μm^2 surface), whereas the *RMS* value of the plateau between the cracks was about 1.25 nm (Fig. 5,c).

The heating of the samples at $T_A = 1000$ °C induced also the development of the cracks (Fig. 5,d). Along with this, the number of

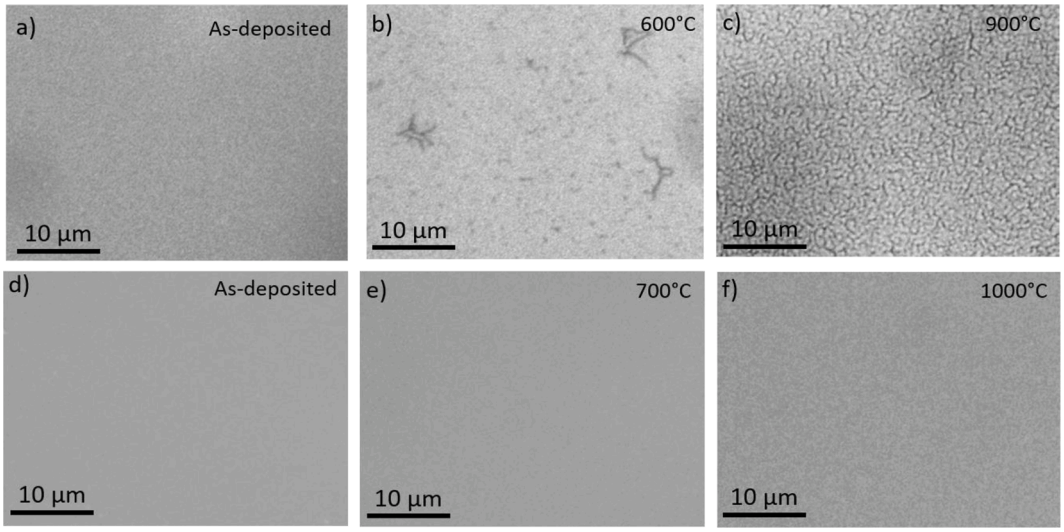

Fig. 4. Surface images obtained with an optical microscope for as-deposited and annealed Er_2O_3 films grown with thermal and plasma-assisted approaches using Er $(CpMe)_3$ (a–c) and $Er(tmhd)_3$ (d–f) precursors, respectively. Annealing temperatures are mentioned in the figures.

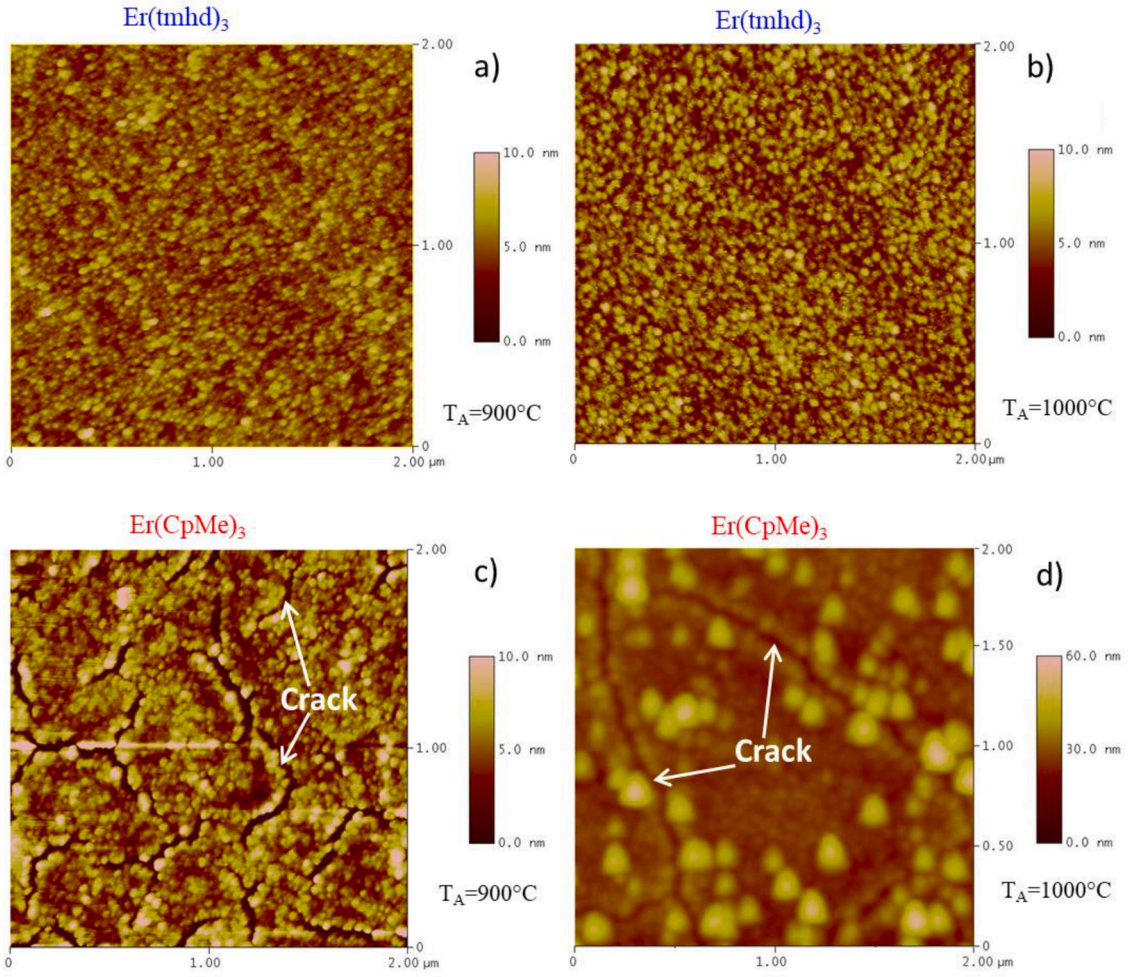

Fig. 5. AFM images of the surface of Er_2O_3 films grown with the plasma assisted approach (a, b) and the thermal approach (c, d) and annealed at 900 °C (a, c) and 1000 °C (b, d).

grains on the plateau between the cracks increases. Two types of the grains can be seen on the top surface of the plateau, i.e. small gains with average size of about 100–140 nm and large grains with the lateral sizes of 200–250 nm. It would be noted that the measured depth of the cracks' could be underestimated because of the curvature radius of the *AFM* tip. *TEM* results presented in the following sections, support this statement

and show that in some regions the cracks penetrate down to the substrate surface (Fig. 6S, see supplement materials).

The results presented above show that the films grown with the plasma-assisted approach are structurally more stable upon anneal treatment. However, in both cases, the formation of grains on the film surface can be the result of its crystallization. Due to mismatching in lattice parameters between Er_2O_3 film (for cubic Er_2O_3, a =1.054 nm) and underlying Si substrate (for cubic Si, a =0.543 nm), one can expect that films are compressively stressed. Thus, an annealing can result in their relaxation via the formation some cracks. However, in the films grown with the plasma assisted approach, such stresses can be smaller than in their counterparts prepared with the thermal approach. One of the reasons could be the higher growth rate per cycle in the thermal approach (about 80–100 pm/cycle against 15–20 pm/cycle for plasma assisted approach). The presence of OH- or CH-groups as well as other volatile complexes (that were not completely removed during the deposition) can be an additional reason of this phenomenon. Thermal treatment at high T_A values can also provoke the diffusion and desorption of such complexes and, as a consequence, the formation of cracks or even film delamination from the substrate. Besides, the formation of silicates allowing a decrease in the mismatching between the film and underlying substrate is also possible. One can assume that the mechanism of the film relaxation could be different for the films grown with different approaches.

3.3.2. *XRD data*

In order to see the effect of annealing on the film crystallization, *XRD* study was performed for the samples mentioned above and the corresponding patterns are plotted in Fig. 6. The comparison of *XRD* data with the standard cubic Er_2O_3 patterns [29,30] shows that the films are crystallized in cubic phase, even after deposition. Both grazing and Bragg-Brentano geometries support this statement (Fig. 6,a and b, respectively). As-deposited films grown at 300 °C show the most intense peaks in the 2θ = 20-60° range at 2θ = 23.48° (2 1 1), 33.73° (2 2 2), 39.10° (4 0 0) and 56.82° (4 4 0) (Fig. 6), that are shifted towards lower angles in comparison with standard values reported for cubic Er_2O_3. This shift is most probably due to the mismatch between the lattice parameters of the film and the underlying substrate. Indeed, for standard Er_2O_3, the a_{Er2O3} = 1.054 nm value is about twice larger than the unit cell parameter of Si substrate ($2a_{Si}$ = 1.086 nm). However, a small negative mismatch for the Er_2O_3 film can generate stress. Thus, for as-deposited films, it is found that a_{Er2O3} = 1.0617 nm and the microstrains are about ~0.74%.

Thermal treatment of the films at high temperatures causes further their crystallization as well as strain relaxation. Indeed, the T_A increase up to 1000°C stimulates some narrowing of *XRD* peaks and their gradual shift towards higher angles, i.e. 2θ = 24.06° (2 1 1), 34.12° (2 2 2), 39.64° (4 0 0) and 57.36° (4 4 0) (Fig. 6,b), approaching the values of standard cubic Er_2O_3. The highest intensity of the peak at 2θ = 33.73° (2 2 2) is the evidence of the preferred orientation of the film following the [111] direction. The analysis of *XRD* data revealed the gradual decrease of the lattice parameters down to 1.057 nm and the increase of coherent domain size from ~9 nm up to ~14 nm as well as stress relaxation down to 0.17%. No any other Er_2O_3 phases are identified in the films annealed at $T_A \leq 1000$ °C. For T_A = 1100 °C, additional *XRD* peaks appear at 2θ = 35.36° and 38.15° that can be assigned to Er_2SiO_5 phase (PDF card No. 52-1809). An appearance of this phase is caused by the diffusion of silicon atoms from underling substrate in the film volume due to the high temperature applied. The appearance of silicate phase was also reported for Er_2O_3 thin films by other groups [19,20],.

Thus, *XRD* data confirm the conclusions drawn from ellipsometry data and *AFM* observations. However, to obtain more information about the factors that can result in the evolution of the refractive index and of the film thicknesses, *FTIR* experiments were carried out. Besides, this method permits to detect the OH-groups (if any) and the formation of SiO_2 or Er-silicate phases in the films described above.

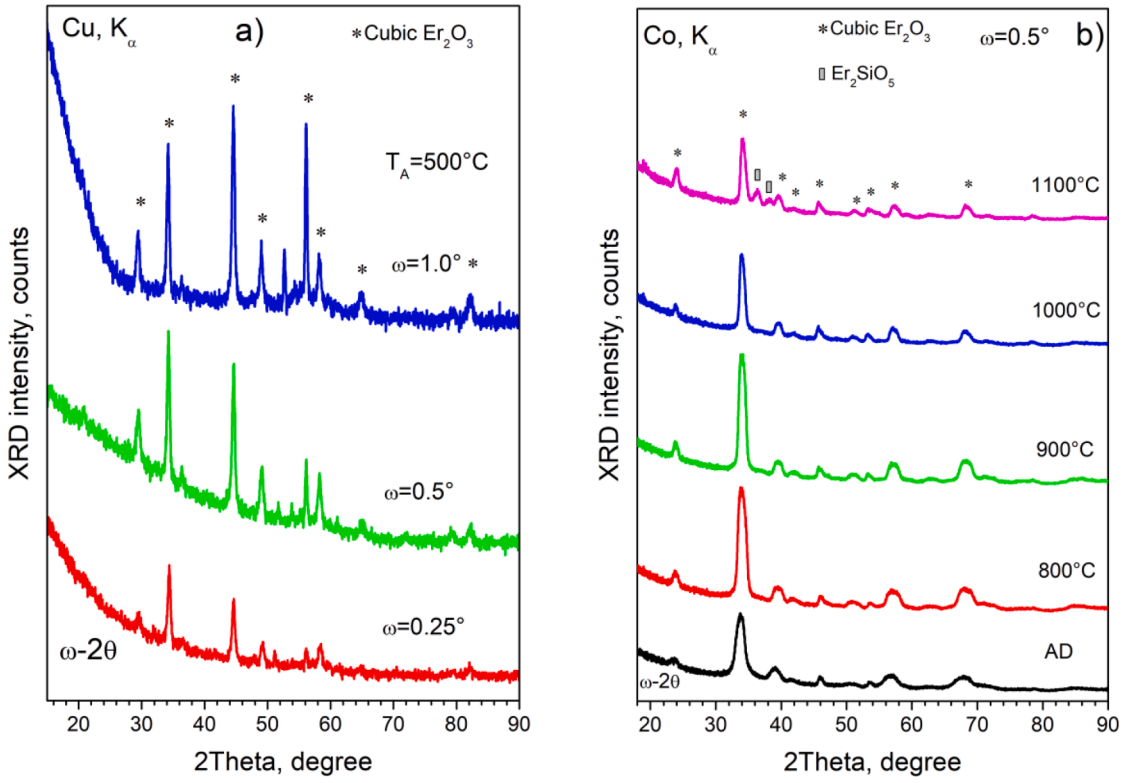

Fig. 6. Grazing-incidence XRD patterns of Er_2O_3 films grown with plasma-assisted (a) and thermal (b) approaches. The conditions of XRD experiment: (a) ω = 0.25, 0.5 and 1.05°; excitation source – Cu K_α = 1.5406 Å, the patterns are recorded for films annealed at 500 °C; (b) ω = 0.5°; excitation source – Co K_α = 1.78897 Å, XRD patterns are recorded for as-deposited and annealed at T_A = 800–1000 °C films. In both figures, the curves are shifted vertically for clarity.

3.3.3. Evolution of FTIR spectra

The *FTIR* spectra of the as-deposited Er_2O_3 film grown different *ALD* approaches were found to be similar that is an evidence of their microstructural similarity. The detailed analysis of FTIR spectra recorded for mid-IR spectral range for the samples grown with $Er(CpMe)_3$ precursor was performed by us earlier in Ref. [42]. Hereafter, the spectra of the films grown with plasma-assisted *ALD* approach are presented.

Fig. 7 shows FTIR spectra of Er_2O_3 films grown with $Er(tmhd)_3$ precursor detected in mid-IR spectral range under normal and 60° incidences of excited light. The signals of Er-O vibrations in the 400–650 cm^{-1} range are seen (Fig. 7,a). Besides, the modes caused by C-H vibrations as well as H_2O and OH-related ones are present (Fig. 7,b). These vibration bands could originate from the byproducts remained in the films after precursor decomposition and oxidation. An annealing resulted in the decrease of these signals up to their vanishing for T_A >900 °C.

Apart from this, in the films annealed at T_A ≥700°C, Er-O related peaks become to be well-defined, being sharper for higher T_A values (Fig. 7). Furthermore, additional Si-O-Si bands peaked at about 1250, 1080 and 820 cm^{-1} appear. Since the films were grown on Si substrate covered with thermal 5-nm SiO_2 layer, the increase of the magnitude of the Si-O-Si band peaked at 1250 cm^{-1} is the evidence of the increase of SiO_2 layer thickness that can be caused by the oxygen diffusion from the film towards film/Si substrate interface. Similar phenomenon was reported in [[36,43]. It was also shown that oxygen diffusion is 5–6 orders of magnitude faster along the grain boundaries than in the bulk [44] that can explain the increase of SiO_x layer thickness. Further T_A increase results in the decrease of the contribution of Si-O-Si related bands as well as in the appearance and enhancement of Si-O-Er bands in the 800–1100 cm^{-1} spectral range. The presence of the Si-O-Er bands could originate from the formation Er silicate phase due to interaction of the film with underlying substrate via Er diffusion towards film/substrate interface and/or Si diffusion in film volume.

Similar morphology evolution for the films grown with two approaches is demonstrated by Fig. 8 where FTIR spectra are compared for mid-IR and far-IR spectral ranges. It is seen that as-deposited films of both types show Er-O related vibration bands in the 100–700 cm^{-1} range. Their narrowing occurred upon film annealing at $T_A \geq 900$ °C indicating crystallization of the films which is in agreement with the *XRD* results. At the same time, the comparison of the shape of Si-O-Er related peaks revealed that these peaks are sharper for the films grown with plasma-assisted *ALD*. Thus one can assume that more pronounced crystallization occurs in the films grown with $Er(tmhd)_3$ precursor.

The formation of Er silicate phase was reported in Refs. [39,43,45]. It was shown that this process can require a short annealing time, for instance, it can occur upon rapid thermal annealing (at 600–900 °C for 30 s). As for the Er_2O_3 films studied in this work, they are grown as crystalline. The presence of grain boundaries can be a reason not only for fast oxygen diffusion from the film towards film/substrate interface upon annealing, but also for the diffusion of other species, for instance, Si atoms from the substrate (or interface layer) in the film volume.

Since in our case annealing time was longer (30 min) the diffusion process can be very significant. Besides, high-temperature annealing stimulates further film crystallization that can promote such diffusion via the appearance of additional grain boundaries. Meanwhile, the broad featureless Si-O-Er vibration band as well as nearly unchangeable intensity of Si-O-Si vibration band peaked at 1250 cm^{-1} detected in the films grown with $Er(CpMe)_3$ and annealed at $T_A \leq 1000$ °C could be caused by the difference in the diffusion processes and film crystallization in comparison with similar processes occurring in the films grown with $Er(tmhd)_3$ precursor and submitted to the same thermal treatment. The higher ratio of the magnitudes of Er-O bands to that of Si-O-Si vibrations observed for the films grown with $Er(CpMe)_3$ demonstrates the better crystallization of Er_2O_3 original layer and lower contribution of Er silicate crystallization that can be caused by the competition of the oxygen diffusion towards film/substrate interface and out-diffusion of byproducts (for instance, OH-groups) whose presence was detected in as-grown films [42]. The crystallization of Er silicate phase was revealed

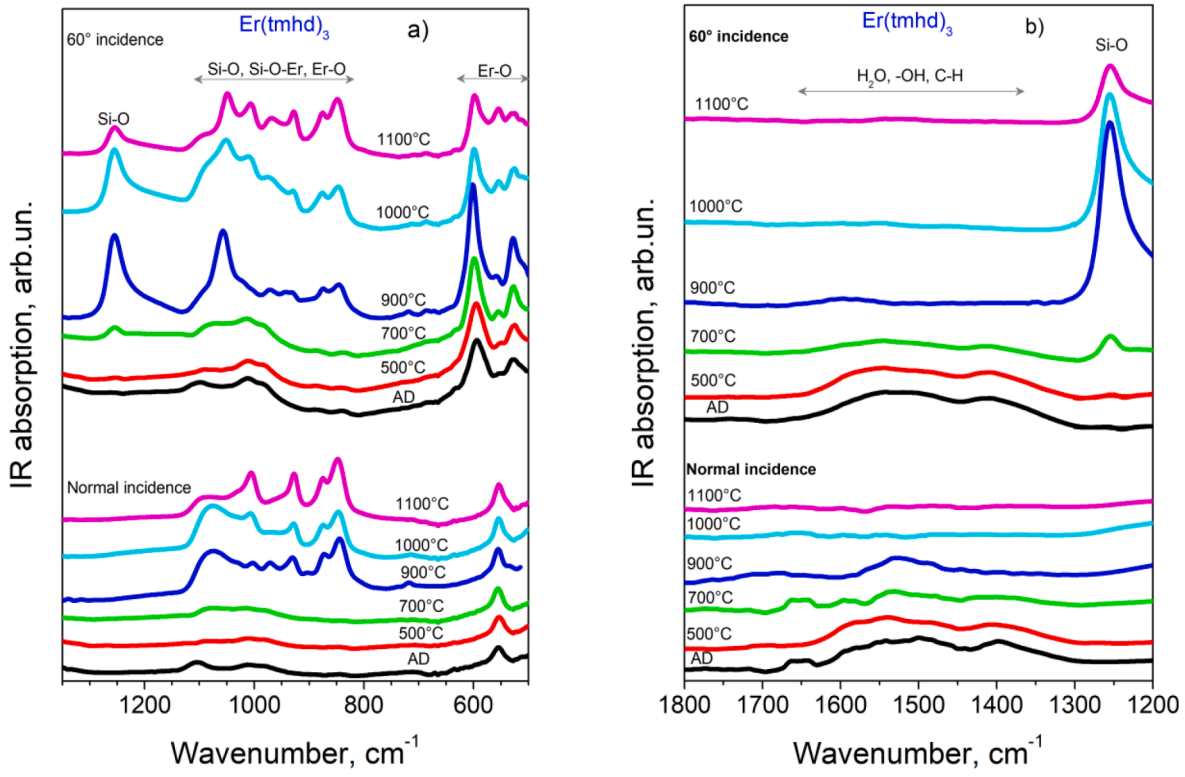

Fig. 7. FTIR spectra of Er_2O_3 films grown with plasma assisted ALD versus T_A recorded with normal and 60 incidence of excitation light and presented for different spectral ranges.

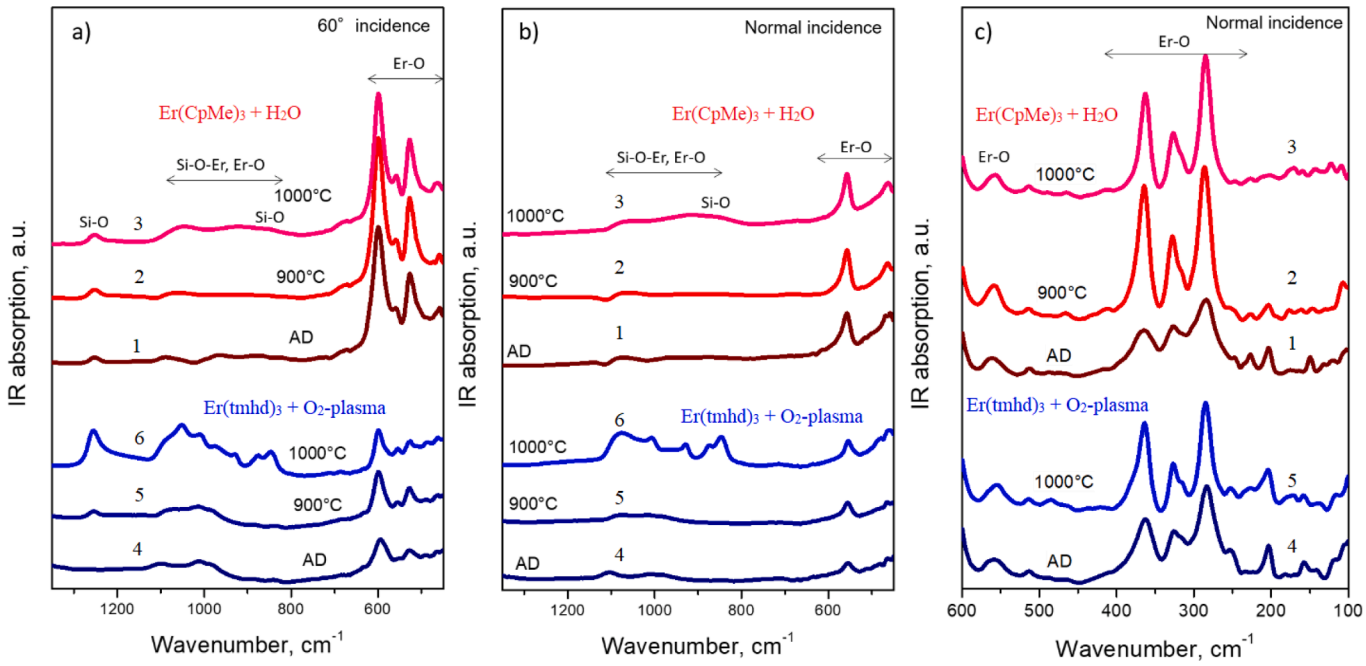

Fig. 8. Comparison of FTIR spectra of as-deposited (AD) and annealed at different temperatures Er_2O_3 films grown with $Er(CpMe)_3$ by the thermal ALD and with $Er(tmhd)_3$ by the plasma assisted ALD. The spectra were recorded with normal and 60° incidence of excitation light and were shifted vertically in the figures for the clarity. Annealing temperatures are mentioned in the figures.

for the films annealed at T_A = 1100 °C only whereas such process became to be significant already for the films grown with $Er(tmhd)_3$ precursor at T_A = 900 °C (Figs.7 and 8).

An analysis of these samples using the *TEM* technique is necessary to get insight on the spatial localization of SiO_x and/or Er silicate phases in the samples annealed at high T_A. Earlier we have observed cross-sections of the films grown with thermal *ALD* and corresponding results were discussed in [42]. Following that, the *TEM* results for the films grown with plasma-assisted ALD approach will be presented and compared with those obtained for the films grown by thermal ALD and submitted to the same annealing treatment.

3.3.4. *Microstructure of the films*

Fig. 9 represents, as an example, a cross-sectional view of the film grown with $Er(tmhd)_3$ and annealed at T_A = 900 °C. The film thickness is about 72 nm (Fig.9,a) that supports the thickness value obtained by the ellipsometry spectra fitting (Fig. 3,b).

Dark field and bright field *TEM* images show that only the upper part of the film (over a thickness of about 53 nm) is crystalline. The dark field image was obtained from (200) spots of Er_2O_3. The bottom part has a uniform contrast that is characteristic for an amorphous material. It is seen that the grains are elongated following the growth direction with a dimension of about 53 nm for the largest ones and their average width is about 15 nm (Fig. 9,a and b).

Fig. 9,c and d are HRTEM images of enlarged regions indicated in Fig. 9,b by rectangular dashed boxes. The bottom region (about 19 nm thick) is clearly amorphous since no lattice fringes are visible in Fig. 9,c. By contrast, the enlarged top surface of a typical grain is crystalline and the FFT pattern, shown in inset, is consistent with the Er_2O_3 cubic phase. One can also notice the significant film roughness corresponding to the top of the elongated grains as observed by *AFM* method (Fig. 5). The comparison of these data with *FTIR* spectra allows assuming that this amorphous layer is an Er silicate layer caused by Si diffusion from the substrate. This has been confirmed by EDX measurements (see below).

Fig. 10 shows HRTEM images of the Er_2O_3 film grown with the plasma-assisted approach and annealed at 1100 °C. The upper part of the film keeps its cubic Er_2O_3 structure (Fig. 10,a). Indeed, the FFT in inset is consistent with a [111] projection of a bixbyite structure (centered cubic structure) with lattice parameter a =10.53 Å corresponding to the cubic Er_2O_3 structure.

Fig. 10,b clearly evidences the presence of a thicker silica layer (about 7.5 nm) compared to that (about 4.5 nm) observed upon 900 °C anneal treatment. On the top of this silica layer, a crystalline Er_2SiO_5 layer (about 20 nm thick) with elongated grains lying parallel to the substrate is found. The FFT in inset attests of the monoclinic structure of this phase with the following characteristics: a = 14.32 Å, b = 6.69 Å, c = 10.35 Å and β = 122.33°. These results are in agreement with the XRD data. The appearance of some pores (voids or cavities) located between the Er_2O_3 and Er_2SiO_5 layers is also detected which can be caused by desorption of residual chemical species from the film upon annealing as well as stresses relaxation in the films. However, this effect is less pronounced for the films grown with the plasma-assisted approach than with thermal *ALD* [42].

To confirm the silicate nature of the bottom part of the film, EDX mapping were performed. Fig. 11 is a panel of chemical maps (Er, Si and O elements) of the cross section of the film annealed at 1100 °C. The STEM HAADF image in Fig. 11,a clearly shows the three different regions of the film: the bottom 7.5 nm thick silica layer, the intermediate erbium silicate layer (about 25 nm thick) and the upper erbium oxide layer (about 40 nm thick). Note the small dark regions in the middle of the film in Fig. 11,a. These latter are the voids evoked previously.

The various contrasts of the chemical maps and more particularly those of Er and Si maps, confirm the previous statements: the Er map shows a brighter region at the upper part of the film confirming the higher content in Er in this region (erbium oxide film). The Si map clearly depicts the presence of Si at the bottom part of the film which is consistent with the silica and the erbium silicate layers in this region. A quantitative approach reveals that one have approximately twice the amount of Er compared to the Si content which is consistent with the Er_2SiO_5 phase. These findings support the conclusions made from *FTIR* spectra analysis (Figs. 7 and 8) as well as from ellipsometry data (Fig. 3). The evolution of film morphology and crystalline structure can also affect light emitting properties of the films. In particular, photoluminescence will be discussed in the next section.

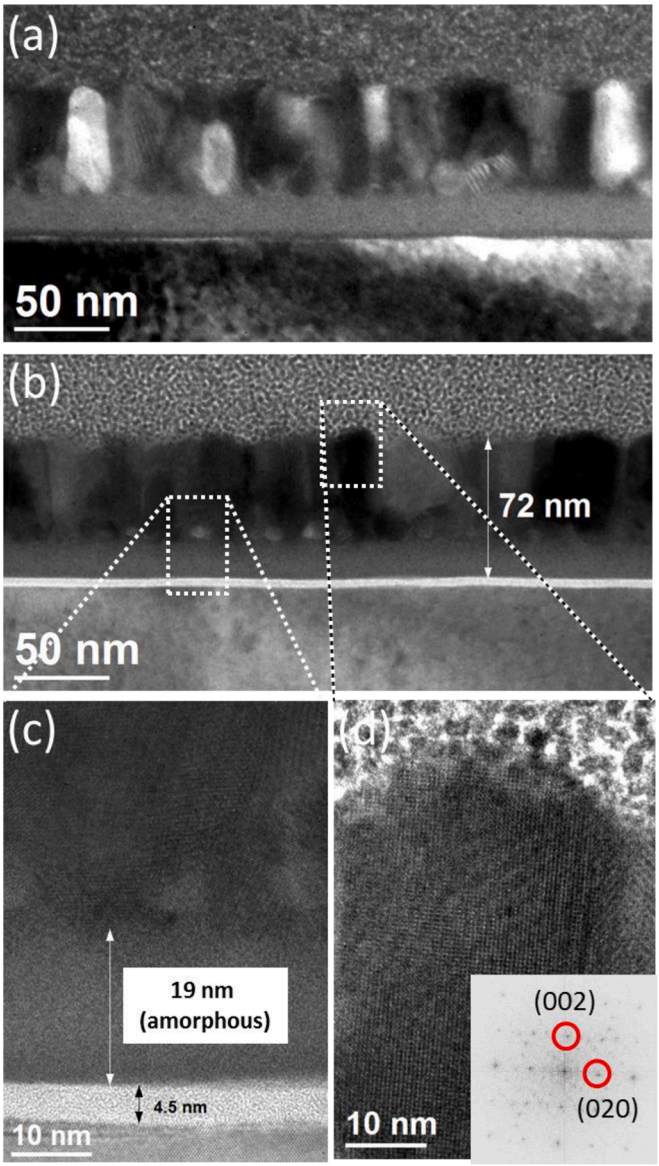

Fig. 9. Dark (a) and bright (b) fields TEM images of a cross sectional view of the Er_2O_3 film grown with the plasma-assisted approach and annealed at T_A = 900 °C. High-resolution TEM images of the bottom region of the film (c) and the top of the film (d). The inserted FFT pattern in (d) is in agreement with the cubic structure of Er_2O_3.

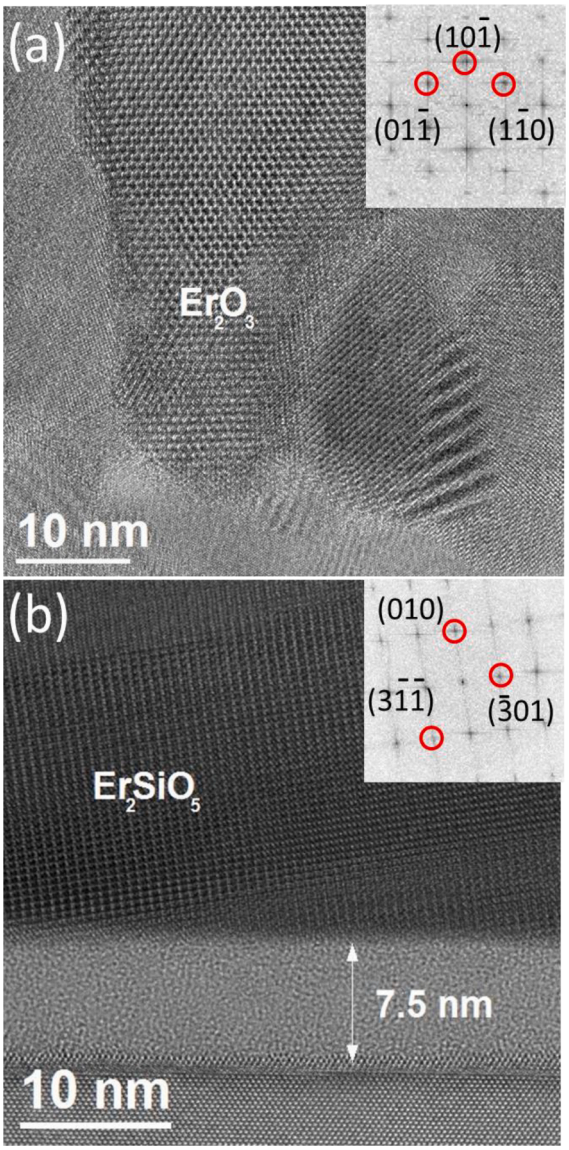

Fig. 10. (a) HRTEM image taken from the upper part of the film grown with the plasma-assisted approach and annealed at 1100 °C. It shows the presence of crystalline grains having the cubic structure of Er_2O_3. (b) HRTEM image of the bottom region of the film revealing the presence of a crystalline Er silicate phase.

3.3.5. *Photoluminescence properties of the films*

Light emission of bulk erbium oxide is caused by the native defects (for instance, oxygen vacancies) [40,41,42]. Besides, Er^{3+} ions can give the contribution in luminescence spectrum. In this regard, light emitting properties of the films investigated will be considered taking into account contribution of carrier recombination via defects and via Er^{3+} ions. The difference between them can be made using different excitation light wavelengths. Indeed, the use of non-resonant excitation for Er^{3+} ions can allow separating *PL* bands related to the Er_2O_3 host defects and Er^{3+} ions. Besides, it the use of non-resonant excitation for Er^{3+} ions can help to determine the role of the defects as the sensitizers of Er^{3+} ions similar to the case described in Refs. [39,46]. The *PL* emission of Er^{3+} ions can be directly studied under resonant excitation. The comparison of these approaches will permit us to get insight into the *PL* mechanism in the films investigated.

To observe Er^{3+} *PL* emission, the spectra were recorded under "resonant" excitation corresponding to the Er^{3+} absorption at 488 nm ($^4I_{15/2}\rightarrow{}^4F_{7/2}$ transition) and 532 nm ($^4I_{15/2}\rightarrow{}^4H_{11/2}$ transition). Two main bands in the visible range were detected due to $^4F_{9/2}\rightarrow{}^4I_{15/2}$ (650–700 nm) and $^4I_{9/2}\rightarrow{}^4I_{15/2}$ (780–830 nm) optical transitions [48].

In the as-deposited films, the Er^{3+} related peaks were broad testifying some disorder in the film volume. This broadening was more pronounced in the films grown with thermal *ALD* approach [42]. Annealing at T_A = 500–900 °C show sharp Er^{3+} peaks (Fig. 12,a and b) that confirms the presence of Er^{3+} ions in the crystalline host. Further T_A rise up to 1100 °C results in the appearance of broad *PL* bands peaked near 620 and 700 nm, being overlapped with Er^{3+} *PL* bands (Fig. 12).

The comparison of the evolution of structural and light emitting properties of the films permitted to assume that these broad *PL* components are due to some defects of Er silicate phase which formation was more pronounced in the films grown with the plasma assisted *ALD* approach. This finding is supported by the *FTIR* data and structural evolution discussed above.

According to *PL* data,there are, at least, two different excitation and radiative channels in the films studied. One of them is ascribed to Er_2O_3

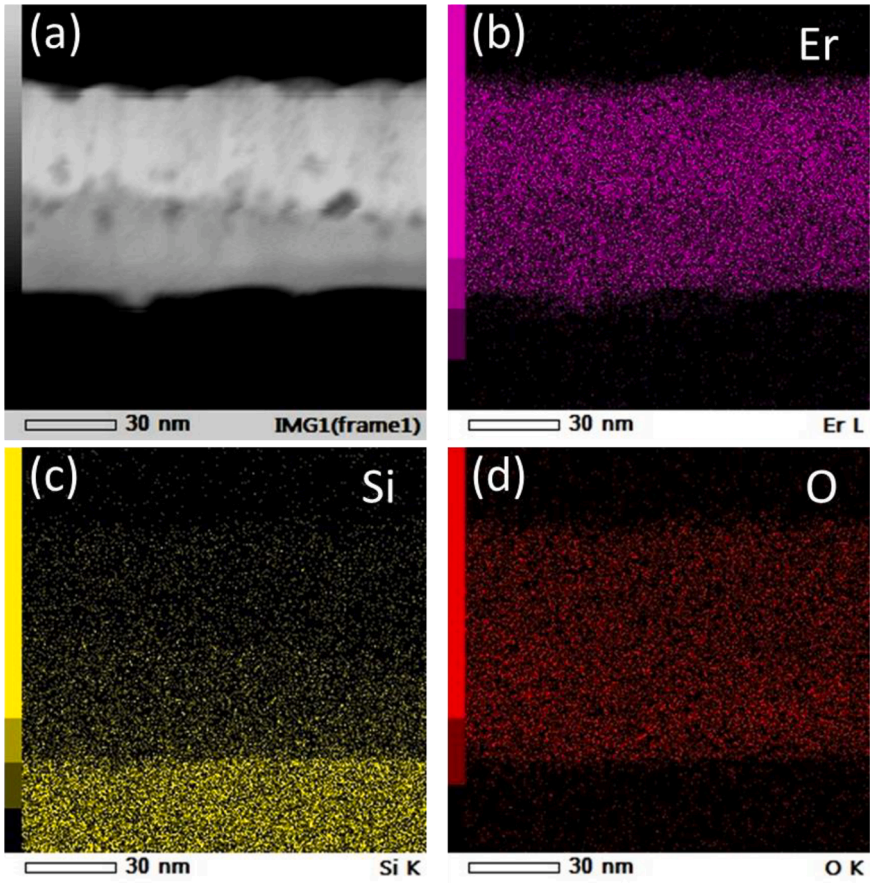

Fig. 11. (a) STEM HAADF image of the cross section of the Er_2O_3 film grown with the plasma-assisted approach and annealed at 1100 °C; (b) Er, (c) Si and (d) O chemical maps of the same region.

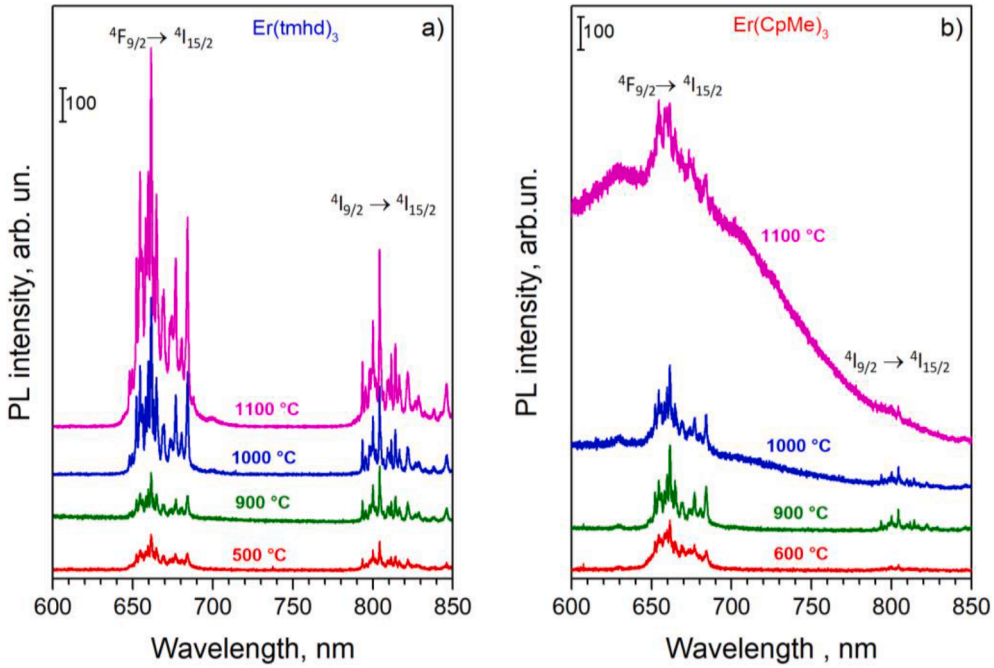

Fig. 12. PL spectra of as-deposited and annealed films grown with plasma-assisted (a) and thermal (b) approaches. The **luminescence** was excited with a 532-nm line of Nd:YAG laser source at room temperature.

host (for instance, its native defects as oxygen vacancies) while the other can be linked to intra-4f shell transitions of Er^{3+} ions [42]. The contribution of Er_2O_3 host defects in *PL* spectrum is significant under ultraviolet excitation. At the same time, the use of visible excitations (for instance, 488 or 532 nm) permits the contribution of Er^{3+} ions in *PL* spectrum to be revealed (Fig. 12).

Fig. 13 shows *PL* spectra recorded for Er^{3+} and more particularly its $^4I_{13/2}\rightarrow{}^4I_{15/2}$ optical transition where the contribution of oxygen vacancies was prevented. It is seen that with T_A rise up to 1000 °C, Er^{3+} *PL* intensity increases showing a saturation behavior. However, further T_A increase (up to 1100 °C) results in Er^{3+} *PL* enhancement. This effect can be caused by the increase of Er^{3+} neighbor distance in Er silicate phase and, as a consequence, by the reduction of the concentration quenching of Er^{3+} *PL* emission. Another reason for *PL* enhancement could be the rise in the number of emitting centers, i.e. the increase of the number of "optically active" Er^{3+} ions in the silicate phase.

In order to obtain information about the contribution of host defects, *PL* spectra were recorded under ultraviolet excitation (Fig.14a). It is seen that under the excitation with 360 nm light (non-resonant for Er^{3+} ions), the *PL* spectrum is broad and featureless and it can be ascribed to the Er_2O_3 host defects as oxygen vacancies. At the same time, under resonant excitation (378 nm), corresponding to the $^4I_{15/2}\rightarrow{}^4G_{11/2}$ absorption for Er^{3+} ions, permit to detect sharp peaks related to Er^{3+} *PL* emission due to $^2G_{7/2}$, $^2G_{9/2}\rightarrow{}^4I_{15/2}$, $^2K_{15/2}\rightarrow{}^4I_{15/2}$ and $^2H_{9/2}\rightarrow{}^4I_{15/2}$ transitions. Similar Er^{3+} peaks are detected under excitation with 488 and 520 nm (Figs. 12 and 13).

Additional arguments towards the potential energy transfers from host defects to Er^{3+} ions can be obtained from *PL* excitation spectra recorded for the same films (Fig. 14,b). It turns out that the *PLE* spectra recorded for 550 and 564 nm detection wavelengths (Fig. 14,b, curves 1,2) are similar to the optical absorption of Er_2O_3 powder (Fig. 14,b, curve 3) that is the evidence of the direct excitation via Er^{3+} ions. Furthermore, some broad background in the *PLE* spectra is also distinguished that may originate from some contribution of oxygen vacancies in the excitation process . The comparison of absorption spectrum and *PLE* ones recorded at 400 nm wavelength is shown for the films annealed at 1000°C (Fig.14,b, inset). The spectra's behaviors are similar, with the exception that the *PLE* spectrum has some additional bands (or shoulders) near 270 and 320 nm. These bands could be caused by self-trapped excitons and host defects, such as oxygen vacancies, complexes of defects, etc. that can contribute in *PL* emission via charge-transfer band. These *PLE* features are similar to those observed for other Er-doped oxides and silicates [21,42]. However, no significant energy transfer is observed between vacancies and Er^{3+} ions meaning that native defects of Er_2O_3 host were not efficient sensitizers of Er^{3+} emission in the films investigated.Besides, in the films grown with thermal approach, the presence of residual OH groups was observed in as-deposited films. It is known that the Er^{3+} *PL* emission can be quenched via $Er^{3+}\rightarrow$OH interaction [49]. At high hydroxyl concentrations, direct resonant energy transfer from the excited Er ion towards OH served as an effective traps. At low OH concentration, fast energy transfer from ion to ion via the Forster mechanism could cause the migration of the excitation towards OH^- groups, where multi-phonon assisted decay to the oxide matrix. Besides, rare-earth concentration is one of dominant factors for cooperative energy transfer. In our films grown with thermal approach both possibilities could be realized because of high Er content. Since annealing treatment results in the reduction of the number of hydroxyl groups, one can expect increasing in *PL* intensity of Er^{3+} ions. However, even small amount of OH groups at 900-1000°C (below 10^{-4} molar fraction) can quench Er^{3+} *PL* emission significantly [49]. This fact could explain higher intensity of rare-earth *PL* in the films grown with plasma assisted approach. Apart from this, high-temperature annealing stimulated formation of Er silicate phase. An appearance of weak oxygen bonds, neutral oxygen vacancies, and Si=O states result in the increasing of the *PL* emission in the 320-600 nm spectral range. Both *PL* and *PLE* spectra of these defects are broad; as a consequence, these defects can be efficient sensitizers of Er^{3+} *PL* emission (Fig. 13). This assumption is in agreement with the results reported for the Er^{3+} emission in Er-doped silicon rich oxide in Ref. [50].

4. Conclusions

This work demonstrates the influence of the nature of Er precursors on the morphology and optical properties of Er_2O_3 films by atomic layer

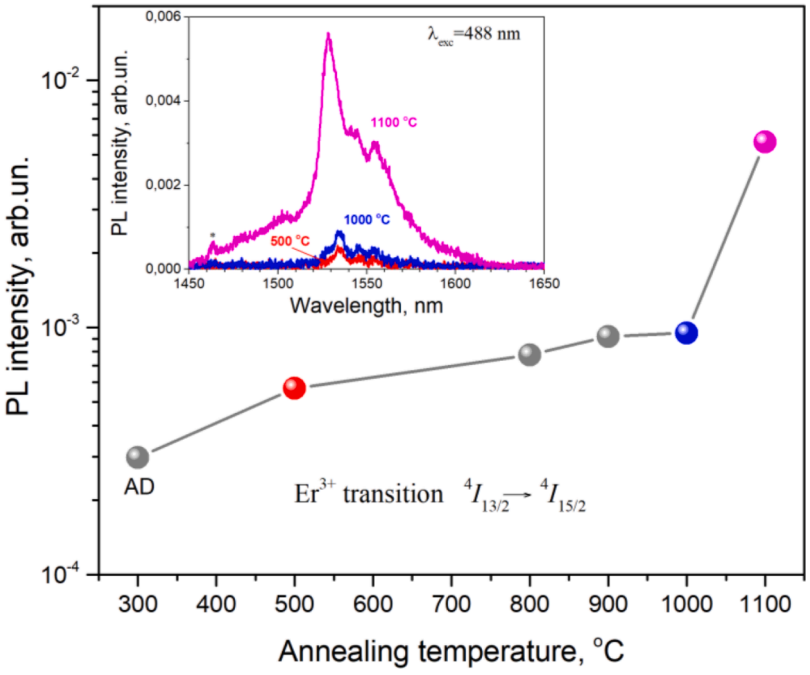

Fig. 13. Effect of annealing temperature on the Er^{3+} PL intensity of the films grown with plasma-assisted ALD. PL evolution is shown for $^4I_{13/2}\rightarrow{}^4I_{15/2}$ transition. PL spectra of the films annealed at 500, 1000 and 1100 °C are presented in the inset. The spectra were recorded at room temperature with a 488 nm excitation light source.

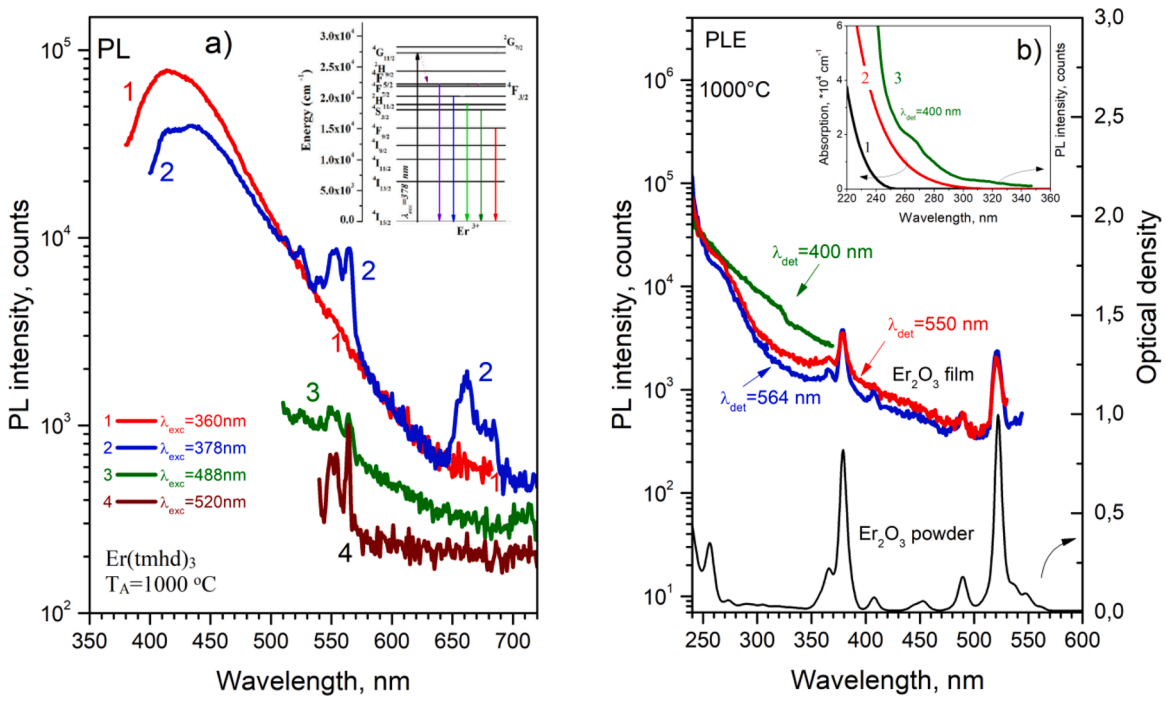

Fig. 14. (a) PL spectra of Er_2O_3 film film prepared with plasma-assisted approach and annealed at 1000 °C. The excitation wavelength is 360 nm (1), 378 nm (2), 488 nm (3) and 520 nm (4); (b) PLE spectra of the same film detected at 400, 550 and 564 nm. The spectrum of optical absorption of Er_2O_3 powder is given for comparison. Inset shows absorption spectra (1,2) and PLE spectrum detected at 400 nm wavelength (3) of the as-deposited film (1) and annealed at 1000 °C (2,3).

deposition and submitted to high-temperature annealing. This latter stimulates pronounced film crystallization accompanied by the formation of Er silicate layer near film/substrate interface due to Si out-diffusion from underlying Si substrate. Upon an annealing at 1000–1100 °C, the appearance of Er_2SiO_5 phase in film volume occurs. Light emitting properties of the films are controlled by the competition of carrier recombination via Er_2O_3 host defects (like oxygen vacancies) as well as via intra-4f shell transitions in Er^{3+} ions. Formation of Er_2SiO_5 phase leads to an enhancement of Er^{3+} emission. Comparison of the evolution of Er^{3+} *PL* emission with annealing temperature for both types of Er_2O_3 films shows the presence of sharper Er^{3+} *PL* peaks in the films grown with plasma assisted approach. This is an additional arguments towards more prominent crystallization process in the films grown with $Er(tmhd)_3$ precursor.

CRediT authorship contribution statement

L. Khomenkova: Conceptualization, Methodology, Investigation, Data curation, Writing – original draft, Writing – review & editing. **H. Merabet:** Funding acquisition, Supervision, Project administration, Validation, Writing – review & editing. **M.-P. Chauvat:** Data curation, Investigation, Visualization. **C. Frilay:** Resources. **X. Portier:** Data curation, Investigation, Visualization, Validation, Writing – review & editing. **C. Labbe:** Investigation, Validation, Writing – review & editing. **P. Marie:** Data curation, Formal analysis, Visualization. **J. Cardin:** Investigation, Formal analysis, Visualization, Validation, Writing – review & editing. **S. Boudin:** Resources. **J.-M. Rueff:** Data curation, Investigation, Visualization, Validation, Writing – review & editing. **F. Gourbilleau:** Funding acquisition, Supervision, Project administration, Validation, Writing – review & editing.

Declaration of Competing Interest

The authors declare that they have no known competing financial interests or personal relationships that could have appeared to influence the work reported in this paper.

Acknowledgements

This work was partially supported by the Normandy Region and European Regional Development Fund (Fonds Européen de Développement Régional (FEDER)) via LUMIERE project as well as partially supported by the CNRS Federation IRMA - FR 3095 and partly supported by the Qatar National Research Fund (QNRF, a member of the Qatar Foundation) via NPRP grant 8-1467-1-268. The findings achieved herein are solely the responsibility of the authors. The authors would like to thank Dr. Nicolas Ratel-Ramond (CEMES, Toulouse, France) for the *XRD* experiments. LK and XP also thanks Franck Lemarié for the samples' preparation by FIB for TEM experiments. XP also acknowledges the "Agence Nationale de la Recherche" (ANR) for the EQUIPEX "GENESIS" grant "ANR-11-EQPX-0020" in the frame of the "Investissements d'avenir" whose funding allowed the acquisition of the FIB equipment.

Supplementary materials

Supplementary material associated with this article can be found, in the online version, at doi:10.1016/j.surfin.2022.102377.

References

[1] R.W. Johnson, A. Hultqvist, S.F. Bent, A brief review of atomic layer deposition: from fundamentals to applications, Mater. Today 17 (2014) 236–246.
[2] L. Hu, W. Qi, Y. Li, Coatings strategies for atomic layer deposition, Nanotechnol. Rev. 6 (2017) 527–547.
[3] H.C.M. Knoops, T. Faraz, K. Arts, W.M.M. (Erwin) Kessels, Status and prospects of plasma-assisted atomic layer deposition, J. Vac. Sci. Technol. A 37 (2019), 030902.
[4] S.M. George, Atomic layer deposition: an overview, Chem. Rev. 110 (2010) 111–131.
[5] K.H. Goh, A.S.M.A. Haseeb, Y.H. Wong, Lanthanide rare earth oxide thin film as an alternative gate oxide, Mater. Sci. Semicond. Process. 68 (2017) 302–315, https://doi.org/10.1016/j.mssp.2017.06.037.
[6] B.P. Gila, J.W. Johnson, R. Mehandru, B. Luo, A.H. Onstine, K.K. Allums, V. Krishnamoorthy, S. Bates, C.R. Abernathy, F. Ren, S.J. Pearton, Gadolinium oxide and scandium oxide: gate dielectrics for GaN MOSFETs, Phys. Status Solidi A 188 (2001) 239.

[7] C. Liu, E.F. Chor, L.S. Tan, A. Du, Epitaxial growth of Sc_2O_3 films on GaN (0001) by pulsed laser deposition, J. Vac. Sci. Technol. B 25 (2007) 754.

[8] W.-H. Kim, W.J. Maeng, K.-J. Moon, H. Kim, Growth characteristics and electrical properties of La_2O_3 gate oxides grown by thermal and plasma-enhanced atomic layer deposition, Thin Solid Films 519 (2010) 362–366, https://doi.org/10.1016/j.tsf.2010.07.108.

[9] H.D.B. Gottlob, M.C. Lemme, T. Mollenhauer, T. Wahlbrink, J.K. Efavi, H. Kurz, Y. Stefanov, K. Haberle, R. Komaragiri, T. Ruland, F. Zaunert, U. Schwalke, Introduction of crystalline high-k gate dielectrics in a CMOS process, J. Non Cryst. Solids 351 (2005) 1885.

[10] W.C. Chin, K.Y. Cheong, Z. Hassan, Sm_2O_3 gate dielectric on Si substrate, Mater. Sci. Semicond. Process. 13 (2010) 303.

[11] M. Losurdo, M.M. Giangregorio, G. Bruno, D. Yang, E.A. Irene, A.A. Suvorova, M. Saunders, Er_2O_3 as a high-*k* dielectric candidate, Appl. Phys. Lett. 91 (2007), 091914.

[12] J. Päiväsaari, M. Putkonen, T. Sajavaara, L. Niinistö, Atomic layer deposition of rare earth oxides: erbium oxide thin films from β-diketonate and ozone precursors, J. Alloy. Compd. 374 (2004) 124–128.

[13] P.-Y. Chen, A.B. Posadas, S. Kwon, Q. Wang, M.J. Kim, A.A. Demkov, J.G. Ekerdt, Cubic crystalline erbium oxide growth on GaN(0001) by atomic layer deposition, J. Appl. Phys. 122 (2017), 215302.

[14] S. Ohmi, C. Kobayashi, I. Kashiwagi, C. Ohshima, H. Ishiwara, H. Iwai, Characterization of La_2O_3 and Yb_2O_3 thin films for high-k gate insulator application, J. Electrochem. Soc. 150 (2003) F134–F140.

[15] K.M. Hubbard, B.F. Espinoza, Corrosion-resistant erbium oxide coatings by organometallic chemical vapor deposition, Thin Solid Films 366 (2000) 175–180.

[16] V. Mikhelashvili, G. Eisenstein, F. Edelmann, Characteristics of electron-beam-gun-evaporated Er_2O_3 thin films as gate dielectrics for silicon, J. Appl. Phys. 90 (2001) 5447–5449.

[17] D. Xue, K. Betzler, H. Hesse, Dielectric constants of binary rare-earth compounds, J. Phys. Condens. Matter 12 (2000) 3113–3118.

[18] S. Saini, K. Chen, X. Duan, J. Michel, L.C. Kimerling, M. Lipson, Er_2O_3 for high-gain waveguide amplifiers, J. Electron. Mater. 33 (2004) 809–814.

[19] M. Miritello, R. Lo Savio, A.M. Piro, G. Franzò, F. Priolo, F. Iacona, C. Bongiorno, Optical and structural properties of Er_2O_3 films grown by magnetron sputtering, J. Appl. Phys. 100 (2006), 013502.

[20] T.M. Pan, C.L. Chen, W.W. Yeh, S.J. Hou, Structural and electrical characteristics of thin erbium oxide gate dielectrics, Appl. Phys. Lett. 89 (2006), 222912.

[21] M. Miritello, R. Lo Savio, F. Iacona, G. Franzò, C. Bongiorno, A. Irrera, F. Priolo, The influence of substrate on the properties of Er_2O_3 films grown by magnetron sputtering, J. Lumin. 121 (2006) 233–237.

[22] M.P. Singh, C.S. Thakur, K. Shalini, N. Bhat, S.A. Shivashankar, Structural and electrical characterization of erbium oxide films grown on Si (100) by low-pressure metalorganic chemical vapor deposition, Appl. Phys. Lett. 83 (2003) 2889–2891.

[23] Y.H. Chang, M.H. Chou, T.J. Wang, Synthesis and photoluminescence properties of erbium oxide thin films prepared by sol-gel method, Ceram. Int. 44 (2018) 163–1167.

[24] M. Miritello, R. Lo Savio, F. Iacona, G. Franzo, A. Irrera, A.M. Piro, C. Bongiorno, F. Priolo, Efficient luminescence and energy transfer in erbium silicate thin films, Adv. Mater. 19 (2007) 1582–1588.

[25] T.H. Phung, D.K. Srinivasan, P. Steinmann, R. Wise, M.B. Yu, Y.C. Yeo, C. Zhu, High performance metal-insulator-metal capacitors with Er_2O_3 on ALD SiO_2 for RF applications, J. Electrochem. Soc. 158 (2011) H1289–H1292.

[26] K. Xu, A.R. Chaudhuri, H. Parala, D. Schwendt, T. de los Arcos, H. Jörg Ostenb, A. Devi, Atomic layer deposition of Er_2O_3 thin films from Er tris-guanidinate and water: process optimization, film analysis and electrical properties, J. Mater. Chem. C 1 (2013) 3939–3946.

[27] STREM (Europe), France; https://www.strem.com/; for Er(CpMe)$_3$ see https://www.strem.com/catalog/v/68-8740/19/erbium_39470-10-5 ; for Er(tmhd)$_3$ see https://www.strem.com/catalog/v/68-8750/erbium_35733-23-4, 2022.

[28] K.J. Eisentraut, R.E. Sievers, Thermogravimetric studies of metal β-diketonates, J. Inorg. Nucl. Chem. 29 (1967) 1931–1936, https://doi.org/10.1016/0022-1902(67)80452-4.

[29] The Crystallography Open Database (COD): an open-access collection of crystal structures, http://www.crystallography.net/cod/COD; Reference code for XRD data of Er_2O_3 is 96-154-1746; compound name: 1541745; 2022.

[30] Joint Committee for Powder Diffraction Data; PDF Card # 01-074-1983.

[31] V.P. Rao, B. Besancon, V. Omarjee, C. Dussarrat, Development of lanthanide precursors as dopants for advanced high-k materials, ECS Trans. 33 (2010) 145–156.

[32] J. Niinistö, T. Hatanpää, M. Kariniemi, M. Mäntymäki, L. Costelle, K. Mizohata, K. Kukli, M. Ritala, M. Leskelä, Cycloheptatrienyl-cyclopentadienyl heteroleptic precursors for atomic layer deposition of group 4 oxide thin films, Chem. Mater. 24 (2012) 2002–2008.

[33] S. Seppälä, M. Vehkamäki, K. Mizohata, W. Noh, J. Räisänen, M. Ritala, M. Leskelä, Comparative study on the use of novel heteroleptic cyclopentadienyl-based zirconium precursors with H_2O and O_3 for atomic layer deposition of ZrO_2, J. Vac. Sci. Technol. A 37 (2019), 010912.

[34] In this work, the R-200-Advanced ALD setup from Picosun Oy (Finland) was used. More details about PICOSUN R-series atomic layer deposition reactors can be found at https://www.picosun.com/product/r-200-advanced/, 2022 [Online].

[35] In this work, silicon wafers from "Sil'tronix Silicon Technologies" (France) were used. More details available at https://www.sil-tronix-st.com/en/silicon-wafer/silicon-wafer-specifications, 2022.

[36] L. Khomenkova, X. Portier, J. Cardin, F. Gourbilleau, Thermal stability of high-k Si-rich HfO_2 layers grown by RF magnetron sputtering, Nanotechnology 21 (2010), 285707 (12pp).

[37] L. Khomenkova, C. Labbe, X. Portier, M. Carrada, F. Gourbilleau, Undoped and Nd^{3+} doped Si-based single layers and superlattices for photonic applications, Phys. Status Solidi A 210 (2013) 1532–1543, https://doi.org/10.1002/pssa.201200942.

[38] L. Khomenkova, N. Korsunska, C. Labbe, X. Portier, F. Gourbilleau, The peculiarities of structural and optical properties of HfO_2-based films co-doped with silicon and erbium, Appl. Surf. Sci. 471 (2019) 521–527.

[39] M.F. Al-Kuhaili, S.M.A. Durrani, Optical properties of erbium oxide thin films deposited by electron beam evaporation, Thin Solid Films 515 (2007) 2885–2890.

[40] H.S. Kamineni, V.K. Kamineni, R.L. Moore II, S. Gallis, A.C. Diebold, M. Huang, A. E. Kaloyeros, Optical and structural characterization of thermal oxidation effects of erbium thin films deposited by electron beam on silicon, J. Appl. Phys. 111 (2012), 013104.

[41] G. Adachi, N. Imanaka, The binary rare earth oxides, Chem. Rev. 98 (1998) 1479–1514.

[42] Y.H. Chang, M.H. Chou, T.J. Wang, Synthesis and photoluminescence properties of erbium oxide thin films prepared by sol-gel method, Ceram. Int. 44 (2018) 1163–1167.

[43] L. Khomenkova, M.P. Chauvat, P. Marie, C. Frilay, F. Lemarié, S. Boudin, X. Portier, N. Ratel-Ramond, C. Labbé, J. Cardin, F. Gourbilleau, Thermally induced evolution of optical and structural properties of Er_2O_3 films grown on Si substrates by thermal atomic layer deposition, Mater. Lett. 263 (2020), 127216.

[44] H. Ono, T. Katsumata, Interfacial reactions between thin rare-earth-metal oxide films and Si substrates, Appl. Phys. Lett. 78 (2001) 1832–1834.

[45] H. Wong, H. Iwai, On the scaling issues and high-κ replacement of ultrathin gate dielectrics for nanoscale MOS transistors, Microelectron. Eng. 83 (2006) 1867–1904.

[46] W. Deqi, Y. Jincheng, Z. Hongsheng, C. Aimin, Li Feng, Leakage current mechanisms of ultrathin high-k Er_2O_3 gate dielectric film, J. Semicond. 30 (2009), 103003.

[47] J. Wang, Y. Xia, Y. Shi, Z. Shi, L. Pu, R. Zhang, Y. Zheng, Z. Tao, F. Lu, 1.54 μm photoluminescence emission and oxygen vacancy as sensitizer in Er-doped HfO_2 films, Appl. Phys. Lett. 91 (2007), 191115.

[48] M. Dammak, D.L. Zhang, Spectra and energy levels of Er^{3+} in Er_2O_3 powder, J. Alloy. Compd. 407 (2006) 8–15.

[49] S. Abedrabbo, B. Lahlouh, A.T. Fiory, Analytical study of thermal annealing behaviour of erbium emission in Er_2O_3-sol–gel silica films, J. Phys. D Appl. Phys. 44 (2011) 315401.

[50] L. Jin, D. Li, L. Xiang, F. Wang, D. Yang, D. Que, Energy transfer from luminescent centers to Er^{3+} in erbium-doped silicon-rich oxide films, Nanoscale Res. Lett. 8 (2013) 366.